

BALLISTIC ELECTRON EMISSION MICROSCOPY

1. INTRODUCTION

The physics of carrier transport through thin films and across interfaces is fundamental to the understanding of microelectronic devices. Ballistic electron emission microscopy, or BEEM, comprises a family of spectroscopies which address the transport and scattering of electrons and holes in multilayer structures. BEEM is based on STM technology and is therefore highly spatially resolved - the typical resolution is about 2 nm. The spectroscopic information which can be extracted from a BEEM measurement is also extraordinarily rich. BEEM, as a result, offers a fundamentally new and powerful way to investigate problems such as Schottky barrier formation, heterojunction band lineups, and quantum confinement.

The physics and chemistry of surfaces have been revolutionized in recent years by an arsenal of new analytical techniques, one of the most exciting being STM. The final properties of an interface, however, often develop only when the interface is fully formed and beyond the range of surface-sensitive techniques. Fully formed interfaces are still best investigated by the conventional tools of current-voltage (I-V), capacitance-voltage (C-V) and internal photoemission or photoresponse (PR) measurements. The principal new technology applied to the problem is the ability to make ever smaller and more uniform structures to minimize statistical averaging of spectral information. BEEM, in a sense, reverses that trend, allowing near-atomic spatial resolution from macroscopic structures.

Since the development of BEEM in 1988, the technique has evolved beyond spatially resolved barrier height measurement to include quantitative interface transport

characterization as well as analysis of band structure, scattering processes, and interface abruptness. In many respects, these are the ideal characteristics for an interface probe. The importance of high energy resolution (principally limited to several meV by thermal effects) and of the ability to perform a true energy spectroscopy cannot be overemphasized. For example, subtle variations in the energies of critical band structure points with temperature, strain and composition may ultimately distinguish different models of interface formation. Such critical points correspond to distinct spectral features in BEEM. With conventional electrical techniques, in contrast, these properties must be extracted from amplitude analysis and extrapolation. Properties such as potential steps at interfaces may be dominated by lateral inhomogeneity, a characteristic which cannot be evaluated at all using averaging techniques.

BEEM employs an STM tip under conventional feedback control to inject ballistic electrons (or holes) into a sample heterostructure. The sample consists of at least two layers forming an interface which presents a potential barrier to the carriers. The top layer and (at least) one other layer are electrically contacted. Figure XX(1) illustrates the simplest possible configuration, with the sample being a metal/semiconductor Schottky barrier (SB) system. The STM tip is biased with respect to the metal layer on the top surface, which serves as system ground. Current flow I_c between the metal base and the semiconductor collector is measured through an ohmic contact on the back side.

As a tip-base bias voltage is applied, electrons tunnel across the vacuum gap and enter the sample as hot carriers. Since characteristic attenuation lengths in metals and semiconductors may be hundreds of Angstroms, many of these hot electrons may propagate through the sample for a long distance and reach the interface before scattering. If conservation laws restricting energy and momentum are satisfied, these electrons may cross the interface and be measured as a current in the collector layer. An n-type

semiconductor is used for electron collection, since the band bending accelerates the collected carriers away from the interface and prevents their leakage back into the base. By varying the voltage between tip and base, the energy distribution of the hot carriers can be controlled, and a spectroscopy of interface transport may be performed.

Figure XX(2) shows the simplest spectrum which may be obtained with BEEM at 'J': O. The theory which describes this spectrum will be discussed later, but the qualitative features may be mentioned here. For tunnel voltages less than the interface barrier height, none of the injected electrons have sufficient energy to surmount the barrier and enter the collector, and the measured collector current is zero. As the voltage is increased to values in excess of the barrier, some of the hot electrons cross the interface into the semiconductor conduction band, and an increase in collector current is observed. The location of the threshold in the spectrum defines the interface barrier height. The magnitude of the current above threshold and the threshold spectrum shape also yield important information on interface transport.

In addition to characterizing conduction band structure, it is also important to probe valence band structure at an interface. A complete description of an interface requires separate knowledge of both conduction and valence band Schottky barrier heights and band alignments. An example of this requirement is provided by strained interfaces, where the semiconductor band gap is perturbed. A spectroscopy of valence band structure may also be performed with BEEM techniques, but utilizing ballistic *holes* as a probe. Since most p-type barriers are relatively low, ballistic hole spectroscopy has required the development of a low-temperature BEEM apparatus. This apparatus has in turn enabled a study of interface properties with temperature, which provides fundamental insights into interface formation mechanisms.

The investigation of carrier transport is also of great importance in solid-state physics, and carrier scattering in materials dominates transport properties. BPEM is a valuable technique for the study of ballistic transport and interface structure, but it does not directly provide a means for an analysis of the carriers which scatter in the base electrode and are not collected. However, a related technique provides a direct spectroscopy of electron and hole scattering. This method is sensitive to the carrier-carrier scattering, and allows the first direct probe of the secondary carriers created by the scattering process. As a spectroscopy of scattering, it is complementary to BPEM, since it provides a way of analyzing *only* the carriers which scatter, and are not observed by the ballistic spectroscopies. Scattering phenomena in metal-semiconductor systems have been investigated, and a theoretical treatment for the collected current has been developed which yields excellent agreement with experiment. The observed magnitudes of the currents indicate that the carrier-carrier scattering process is dominant in ballistic carrier transport.

BPEM has been applied to many interface systems, and important examples will be given in this chapter. A theoretical framework for this technique, and for the corresponding ballistic hole process, will be presented; this theory provides an excellent description of experimental results. The theory which has been developed for carrier-carrier scattering spectroscopy will also be described. Experimental methods particular to BPEM and related techniques will be discussed. Both spectroscopy and imaging of interfaces is possible with ballistic electron and hole probes, and examples of each will be reviewed. The initial application of the new scattering spectroscopy will be presented, as well as preliminary results on the dependence of interface properties on temperature.

2. THEORY

Ballistic electron emission microscopy may be understood by using a simple theoretical model, which may be built upon to include more complicated processes. The essence of the model is the description of the phase space available for interface transport. The simplest case to consider is that of a smooth interface, which dictates conservation of the component of the electron wave vector parallel to the interface (transverse to the interface normal) k_t . Conservation of total energy across the interface provides a second constraint on transport. The process is visualized in Figure XX(3). This diagram may be taken to represent a simplified metal/semiconductor interface system.

A particle incident on a simple potential step, with total energy in excess of the step height, loses a portion of its kinetic energy as it crosses the step, due to a reduction in k_x , the component of k normal to the interface. If the particle is normally incident, the direction of propagation, \hat{k} , is unchanged. For the case of incidence at a non-zero angle to the normal, however, conservation of k_t demands that \hat{k} changes across the interface; i.e. the particle is "refracted". If the angle of incidence is greater than some "critical angle", the particle is not able to cross the interface and is reflected back. This critical angle may be expressed as

$$\sin^2 \theta_c = \frac{E - E_F - eV_b}{E} \quad (I)$$

where the particle total energy in the base is E and the step height is $E_F + eV_b$.

The situation becomes somewhat more complicated for real band structures, if the two regions have dispersion relations which are dissimilar. In this case, the normal and parallel components of the problem are no longer trivially separable. In particular, if E_x is the energy associated with k_x , $E_x > E_F + eV_b$ is no longer the condition for collection. A

change in effective mass) or in the location of the conduction band minimum within the Brillouin zone, alters the critical angle conditions.

For zone centered conduction band minima in both the metal and semiconductor, we can define this critical angle with respect to the interface normal, in terms of electron energy in the base and the potential step $E_F + eV_b$, as

$$\sin^2 \theta_c = \frac{m_{tf}}{m_{xi}} \frac{E - E_F - eV_b}{E + \left[\frac{m_{tf}}{m_{xi}} - \frac{m_{tf}}{m_{ti}} \right] (E - E_F - eV_b)} \quad (2)$$

where m_{xi} and m_{ti} are the components of effective mass in the metal normal to and parallel to the interface, respectively, and m_{xf} and m_{tf} are the corresponding masses in the semiconductor. For evaporated metal base layers which are polycrystalline or of ill-defined orientation, the approximation of an isotropic free-electron mass for the base is made, and the expression reduces to

$$\sin^2 \theta_c = \frac{m_t}{m} \frac{E - E_F - eV_b}{E} = \frac{m}{m} \frac{e(V - V_b)}{E_F + eV} \quad (3)$$

where the second equality is for an incoming electron with $E = E_F + eV$ and m is the free electron mass. This expression, plotted in Figure XX(4), predicts that, for Si(100) or GaAs, with a small component of effective mass parallel to the interface and for $e(V - V_b) \leq 0.3$ eV, this critical angle is less than 6 degrees. Critical angle reflection has important implications for the spatial resolution of interface characterization, since only electrons incident on the interface at small angles can be collected. Thus single scattering events may decrease collected current, but should not degrade spatial resolution. For a 100 Å base layer, at least 20 Å spatial resolution is expected.

The electron injection into the sample by tunneling is treated using a planar tunneling formalism. This description provides simple analytic expressions for the (E, k) distribution of the tunneling electrons and for the total tunnel current. Current across the metal/semiconductor interface is then calculated based upon this initial distribution, by considering the fraction of the total tunnel current which is within the “critical cone”. The vacuum barrier is taken to be square at $V=0$; the WKB form of the tunneling probability $D(E_x)$ is thus written as

$$D(E_x) = \exp\left(-\alpha s(E_F + \Phi - \frac{eV}{2} - E_x)^{1/2}\right), \quad (4)$$

where $\alpha = (8m/\hbar^2)^{1/2} = 1.024 \text{ eV \AA}^{-1/2}$. Tunnel current is given by the standard expression

$$I_t = 2e \int \int \int \frac{d^3k}{(2\pi)^3} D(E_x) v_x \left(f(E) - f(E+eV) \right) \quad (5a)$$

which may conveniently be expressed in terms of integrals over E_x and E_t :

$$I_t = C \int_0^\infty dE_x D(E_x) \int_0^\infty dE_t \left(f(E) - f(E+eV) \right) \quad (5b)$$

where $C = 4\pi me/\hbar^3$ and the integration is over all tip states with $E_x > 0$, E_x is the energy associated with k_x and E_t is that associated with k_t . (It will be convenient in the following discussion to express energies with reference to the bottom of the tip conduction band.) The Fermi function $f(E)$ is defined as

$$f(E) = \left(1 + \exp\left(-\frac{E-E_F}{kT}\right) \right)^{-1} \quad (6)$$

For simplicity, the tip and base are taken to be identical free-electron metals, which will be the assumption for the remainder of this chapter. At $T = 0$, therefore, the appropriate states occupy a half-shell within the tip Fermi sphere between $E = E_F - eV$ and $E = E_F$, as illustrated in Figure XX(5).

A similar expression may be written for the collector current, with the allowed phase space within the tip determined by the critical angle conditions. For the case of m_t less than m , these restrictions on tip states are

$$E_t \leq \frac{m_t}{m - m_t} \left(E_x - E_F + e(V - V_b) \right) \quad (7)$$

$$E_x \geq E_F - e(V - V_b) \quad (8)$$

where E_F is the Fermi energy of the tip, Taking the equalities as limits E_t^{\max} and E_x^{\min} , collector current can be expressed as

$$I_c = RC \int_{E_x^{\min}}^{\infty} dE_x D(E_x) \int_0^{E_t^{\max}} dE_t \left(f(E) - f(E + eV) \right) \quad (9)$$

R is a measure of attenuation due to scattering in the base layer, which is taken to be energy-independent for these energies. If $V_b \gg kT$, as with all examples discussed in this chapter, the second Fermi function $f(E + eV)$ may be neglected. In both Equations YY(5b) and YY(9) the integrals over E_t may be performed analytically; for $T = 0$, this is true also of the integrals over E_x .

Equations YY(7) and YY(8) define a hyperboloid in tip k -space, as shown in Figure XX(5). The integration is performed over this hyperboloidal volume, with the cutoff at higher energies provided by the Fermi function $f(E)$ centered at the tip Fermi level. The threshold shape of the BEEM I_c - V spectrum is determined by the behavior of this k -space volume with voltage, which in turn is determined by the dispersion relation of the collector conduction band. A parabolic conduction band minimum and the assumption of k_t conservation across the interface therefore result in a parabolic threshold shape to the I_c - V spectrum. A similar treatment for I_c can be derived for the case of $m_t > m$.

BEEM spectra are conventionally obtained with the STM operating at constant tunnel current, which normalizes the collected current to the tunnel current and linearizes the BEEM spectrum. In addition, this normalization removes the lowest order effects due to structure in the tunneling density of states which may obscure interface structure. Equation YY(9) for I_c contains factors of s , the tip-sample spacing, which changes with tunnel voltage at constant I_t . Therefore Equation YY(9) will not describe accurately an entire I_c - V spectrum. This effect may be included within the theory in two ways. Equation YY(5b) for $I_t(s, V)$ may be inverted to give $s(I_t, V)$, which is then inserted into Equation YY(9). In practice, this inversion must be done numerically; in addition, the prefactor C , which includes effective tunneling area, must be known. The second method is to treat s as a constant s_0 , but to normalize $I_c(s_0, V)$ by $I_t(s_0, V)$ for each voltage. This requires only that the tunnel *distribution* be relatively insensitive to small changes in s . For the barriers considered here, this assumption is valid, producing errors only on the order of a percent. The expression for I_c then takes the form

$$I_c = RI_t - \frac{E_x^{\text{min}}}{\int_0^\infty dE_x D(E_x)} \frac{\int_0^{E_t^{\text{max}}} dE_t \int_0^\infty dE_x D(E_x) \left(f(E) - f(E+eV) \right)}{\int_0^\infty dE_x D(E_x) \int_0^\infty dE_t \left(f(E) - f(E+eV) \right)} \quad (10)$$

One consequence of the critical angle effect is the sensitivity of BEEM to higher minima in the collector conduction band structure, rather than just the lowest minimum which determines the Schottky barrier height. This is due to the opening of additional phase space for electron transport as electron energy exceeds each minimum in turn. This capability is enabled by the control over injected electron energy provided by BEEM.

The conduction band minima of a particular semiconductor are not in general zone-centered; however, the critical angle restrictions are unchanged provided the minimum is 'on-axis', e.g. a (100) minimum for a (100) surface. The above phase space requirements are therefore appropriate for a metal on Si(100) or Ge(111), although the wave function coupling into these minima may be different. For GaAs of any orientation, off-axis conduction band minima must always be considered. Similar critical angle requirements exist for these off-axis minima, with the center of the critical cone located at an angle to the interface normal given by

$$\sin^2 \theta_0 = \frac{E_{0t}}{E_F + eV_b}, \quad E_{0t} = \frac{\hbar^2 k_{0t}^2}{2m} \quad (11)$$

and k_{0t} is the component parallel to the interface of \mathbf{k}_0 , the location of the minimum. Off-axis minima may be included in the treatment for BEEM, although they do not provide an analytic expression for I_c within the theory discussed here. This case is of

great importance, however, since collection via these minima provides a powerful probe of fundamental quantities such as the (E, k) tunneling distribution, momentum conservation at the buried interface, and carrier scattering.

The foregoing discussion has assumed that all electrons incident on the interface within the critical angle are collected. This classical assumption may not be appropriate for abrupt interfaces, where quantum-mechanical reflection (QMR) must be considered. In this case the integrand of Equation YY(9) must be multiplied by the quantum-mechanical transmission factor appropriate to the potential profile of the interface. Using the approximation of a sharp step potential, this factor may be written as

$$T = \frac{4 \frac{k_{xi}}{m_{xi}} \frac{k_{xf}}{m_{xf}}}{\left(\frac{k_{xi}}{m_{xi}} + \frac{k_{xf}}{m_{xf}} \right)^2} \quad (12)$$

where k_{xi} and k_{xf} are the components of k normal to the interface in the base and collector, respectively. In terms of energies referred to the tip conduction band minimum,

$$T = \frac{\sqrt{\frac{(E_x + eV)(E_x + eV - E_F - eV_b)}{m_{xi} m_{xf}}}}{\left[\frac{E_x + eV}{m_{xi}} + \sqrt{\frac{E_x + eV - E_F - eV_b}{m_{xf}}} \right]^2} \quad (13)$$

which increases as $(V - V_b)^{1/2}$ for V close to the threshold V_b . In the limit of a smooth potential transition from metal to semiconductor, T approaches a step function, and the regime of $(V - V_b)^{1/2}$ behavior becomes small. Alternative expressions for other potentials

may also be used. The analyses of data in this chapter do not include quantum-mechanical reflection terms, although later discussions of ballistic hole spectra will address this point further.

3. HOLE THEORY

The previous section dealt with the investigation of ballistic electron transport and its use as a probe of interface conduction band structure. It was mentioned in the Introduction that n-type semiconductors are necessary for electron collection in order to repel the carriers away from the interface into the collector and prevent leakage back into the base. It is possible to use ballistic *holes*, however, as a probe of valence band structure. The unique aspects of ballistic hole spectroscopy will be discussed in this section.

The implementation of ballistic hole spectroscopy using BEEM techniques is shown in the energy diagram of Figure XX(6) for the case of a metal/semiconductor sample structure. Here, a p-type semiconductor serves as a collector of ballistic holes injected by the STM tip. The tip electrode is biased positively; since injection is through a vacuum tunnel barrier, the injection process must be treated in terms of electron tunneling from the base to the tip. This tunneling process deposits ballistic electrons in the tip and creates a ballistic hole distribution in the base. These distributions are illustrated in Figure XX(6). The hole states retain the same E and k which they had when they were occupied. Note that, since the tunneling is strictly by electrons, the energy and angular distributions of the ballistic holes are determined by the vacuum level. The distribution is therefore peaked towards the base Fermi level.

As a positive voltage is applied to the tip, ballistic holes are injected into the sample structure, As in the ballistic electron case, collector current is zero until the voltage exceeds the barrier height; at higher voltages, collector current increases. It is apparent, however, that the peaking of the hole distribution toward the base Fermi level introduces an asymmetry between the ballistic electron and hole spectroscopes. This asymmetry is shown in Figure XX(6). In BEEM, the portion of the hot electron distribution which is

eligible for collection is toward the higher energies, where the distribution is maximum. For the case of holes, the tail of the distribution is collected. This asymmetry introduces a corresponding asymmetry into a ballistic hole spectrum, as will be discussed later.

The threshold behavior of the ballistic hole I_c - V spectrum, however, is the same as for the case of BEEM. For a hole barrier at $E_F - eV_b$, the critical angle condition, is

$$\sin^2 \theta_c = \frac{m_{tf}}{m_{xi}} \frac{E_F - eV_b - E}{E + \left(\frac{m_{tf}}{m_{xi}} - \frac{m_{tf}}{m_{ti}'} \right) (E_F - eV_b - E)} \quad (14)$$

which may be compared with Equation YY(2). For the case of an isotropic free-electron mass for the base, the expression reduces to

$$\sin^2 \theta_c = \frac{m_t}{m} \frac{E_F - eV_b - E}{E} = \frac{m_t}{m} \frac{e(V - V_b)}{E_F - eV} \quad (15)$$

the second expression being for an incoming hole with $E = E_F - eV$. The ballistic hole I_c - V spectrum threshold has a $(V - V_b)^2$ dependence, in agreement with the ballistic electron case, although the appropriate k -space volume of integration is over states in the base and is quite different from the electron case, as illustrated in Figure XX(7).

4. SCATTERING SPECTROSCOPY THEORY

THEORY FIGURES

- Figure 1 **Energy** diagram for BEEM of a metal/semiconductor Schottky barrier system. (a) Applied tunnel voltage of zero. (b) Applied tunnel voltage eV , in excess of the interface barrier height V_b . For this case, some of the injected electrons have sufficient energy to enter the semiconductor.
- Figure 2 Example of a theoretical BEEM spectrum at $T=0$. Such a spectrum displays a threshold at a voltage equal to the interracial barrier height V_b .
- Figure 3 Schematic diagram representing a particle incident on a potential step of height $E_F + eV_b$, with an initial energy E in excess of this step height. There exists a critical angle θ_c such that a particle incident at an angle in excess of this value is reflected. For an angle of incidence less than θ_c , the particle is transmitted, but is refracted as it crosses the interface.
- Figure 4 Plot of Equation YY(3) representing the case of Au on n-Si(100). For this case, $eV_b = 0.8$ eV, $E_F = 5.5$ eV, and $\text{ret}/m = 0.2$.
- Figure 5 k -space diagram representing the free-electron Fermi sphere of the STM tip, for the case of electron tunneling from tip to sample. For an applied tip-sample voltage V , states within the shell delimited by E_F and $E_F - eV$, and with $k_x > 0$, are eligible to tunnel. If $eV > eV_b$, a subset of these tunneling electrons, defined by a hyperboloid in k -space, satisfy phase space conditions for collection. These volumes are shown here,
- Figure 6 Energy diagrams of ballistic electron and ballistic hole spectroscopes. (a)

In ballistic electron spectroscopy of interface conduction band structure, a hot electron distribution is created, of which the most energetic electrons are available for collection. (b) With ballistic hole spectroscopy of interface valence band structure, a hot hole distribution is created in the base by electron vacuum tunneling. The *least* energetic holes are eligible for collection by the semiconductor valence band.

Figure 7 k-space diagram representing the free-electron Fermi sphere of the sample base, for the case of electron tunneling from sample to tip. For an applied sample-tip voltage V , states within the shell delimited by E_F and $E_F - eV$, and with $k_x > 0$, are eligible to tunnel. If $eV > eV_b$, a subset of these tunneling electrons, defined by the intersection of an ellipsoid and a sphere in k-space, create holes which satisfy phase space conditions for collection. These volumes are shown here.

5. EXPERIMENTAL

The experiments described in this chapter have been performed using a standard STM which has been modified for the particular requirements of BEEM. The most important of these requirements will be discussed in this section.

BEEM is implemented here is a three-terminal experiment; in addition to maintaining tip bias and a single sample bias, individual control of two sample bias voltages is required. This entails controlling base and collector voltages while measuring currents into each of these electrodes. The sample stage on the STM provides contact to both base and collector as shown in Figure XX(1). The sample rests on three iridium pads, one of which touches and provides contact to the base electrode, Contact to the collector is by spring to a back ohmic contact on the semiconductor. The arrangement requires only minor modifications to the existing STM design. The STM design has been discussed in detail previously. Au tips were used for all measurements.

The I_c - V spectra were obtained at constant tunnel current using standard STM feedback techniques. The value of the tunnel current was normally 1 nA. This method has the advantage of linearization of the acquired spectra, as mentioned in the theoretical discussion. All imaging was also performed at constant tunnel current. This maintenance of gap spacing during imaging avoids artificial variations in collector current which would result from changes in tunnel current as the tip is scanned across the surface,

Due to the necessity for measuring small collector currents, a high-gain, low-noise current preamplifier is used, a schematic of which is shown in Figure XX(2). The amplifier provides a gain of 1011 volts/amp in four stages. The reference input of the amplifier is attached to the base electrode and is maintained at ground potential.

Collector current is measured with zero applied bias between base and collector. The effective input impedance of the amplifier is about 10Ω , which is much smaller than the zero bias resistance R_0 of the diode, which, for reasons discussed below, is always greater than about $100 \text{ k}\Omega$. This low input impedance prevents leakage back into the base of electrons which enter the collector. Note that a measurement of collector current by the use of a series resistor would require such a resistor to be at least 108Ω for adequate sensitivity; this large resistance would cause difficulties due to this same leakage back across the interface.

The current amplifier has an inherent input noise, necessitating a large sample source impedance across its terminals. An amplifier input noise of $100 \text{ nV}/\sqrt{\text{Hz}}$ across a source impedance of $100 \text{ k}\Omega$ produces a noise current of picoamps, which is on the order of the signal to be measured. R_0 must exceed this impedance value for adequate signal-to-noise. R_0 may be increased either by reducing the interface area or by a reduction in temperature. The former method is required if R_0 is low due to ohmic regions at the interface. Low temperature measurement is more effective for samples where R_0 is small due to a low interfacial barrier height and a consequent thermionic current. In the thermionic emission approximation, the differential resistance at zero bias can be written

$$r_0 = \left(\frac{dV}{dI} \right)_{V=0} = \left(\frac{eA^*T_a}{k} \right)^{-1} \exp(eV_b/kT) \quad (16)$$

where A^* is the Richardson constant and a is the diode junction area. Diode areas are approximately 0.1 cm^2 , this requires, at room temperature, a Schottky barrier height of at least 0.75 eV . A reduction in temperature from 293K to 77K lowers this value to about 0.2 eV . This dependence of lowest measurable barrier height on temperature is plotted in Figure XX(3). To obtain an equivalent capability for low barrier height measurements, a

reduction in diode area by more than a factor of 10^{10} would be required. In addition to the increase in resist area, low-temperature operation provides increased energy resolution for interface spectroscopy, due to a narrowing of the Fermi edge of the tip. A decrease in Johnson noise of the large tunneling gap resistance also results.

A low-temperature BPEM apparatus, designed for operation at 77K, was developed for use with low-barrier-height interface systems. This includes most important p-type Schottky barriers; 77K operation was therefore required for ballistic hole spectroscopy. All p-type Schottky barrier characterization discussed in this chapter was performed at 77K; for purposes of comparison and for improved energy resolution, selected n-type samples were also characterized at low temperature. Operation at 77K was accomplished by direct immersion of the STM head in liquid nitrogen, with the entire BPEM apparatus enclosed in a nitrogen-purged glove box.

Sample substrates consisted of both Si ($n=2 \times 10^{15} \text{ cm}^{-3}$ or $p=3 \times 10^{15} \text{ cm}^{-3}$) and GaAs ($n=3 \times 10^{16} \text{ cm}^{-3}$) wafers of (100) orientation. MBE-grown GaAs(100) layers ($n=5 \times 10^{16} \text{ cm}^{-3}$ or $p=3 \times 10^{16} \text{ cm}^{-3}$), 1 μm thick, were also used. Si substrate cleaning was by growth and strip of a sacrificial thermal oxide followed by growth of a 100 Å thick gate oxide. GaAs substrate cleaning consisted of solvent rinsing followed by three chemical oxide growth/strip cycles, terminating with the growth of a protective oxide layer. Final sample preparation was performed in a flowing nitrogen environment, using a non-aqueous spin-etch for removal of oxides prior to metal base layer deposition. Samples were transferred directly into ultra-high vacuum without air exposure. All samples discussed here utilize Au base electrodes. Chamber base pressure was 10^{-11} Torr, and was typically 10^{-9} Torr during Au deposition. Unless otherwise stated, Au thickness was 100 Å as determined by crystal oscillator thickness monitor.

Completed samples were characterized by conventional I–V and transferred by load lock into a glove box which is under constant purge by dry flowing nitrogen, where measurements were performed. The glove box also serves to shield the apparatus from light. Light shielding is important during data acquisition, since photocurrents generated by normal laboratory lighting can be orders of magnitude larger than currents due to collection of tunneling electrons. Checkout of the collector current circuitry and sample contacts is conveniently accomplished by admitting a small amount of light into the box.

EXPERIMENTAL FIGURES

Figure 1 BEEM sample mounting scheme. The sample rests on three iridium contact pads over an aperture on a quartz mounting plate through which the STM tip protrudes. One of these pads contacts one end of the base electrode, which is evaporated in a two-lobed pattern. Tunneling is into the other lobe of the base. The collector current is measured through a back-side ohmic contact.

Figure 2 Schematic diagram of the preamplifier circuit used for measurement of collector current. An electrometer-grade amplifier, the OPA-128, is used for the initial gain stage. Total gain is 10^{11} volts/amp.

Figure 3 Minimum measurable barrier height versus temperature calculated from Equation YY(16) for n-Si(100). The criterion for measurement by BEEM is $R_0 = 100 \text{ k}\Omega$, as discussed in the text. For this calculation, $A^* = 252 \text{ A/K}^2/\text{cm}^2$ and the diode area 0.1 cm^2 .

6. BEEM SPECTROSCOPY RESULTS

BEEM has been applied to many different interface systems. Examples will be given in this chapter which illustrate important aspects of BEEM capabilities.

The simplest application of BEEM is to the Au/n-Si(100) SB interface system. Au/Si is important from a device standpoint, and it is known to provide high-quality interfaces and reproducible barrier heights. Figure XX(1) illustrates a representative I_c - V spectrum. A theoretical spectrum which was fit to the data is also shown. The agreement between theory and experiment is excellent; fitting was performed by varying only V_b and R . The vacuum gap parameters used for all Au/n-type semiconductor BEEM data are $\Phi = 3$ eV, $s = 15$ Å and are not varied during fitting. These values may not be precise, since the theoretical spectrum is not sensitive to small changes in Φ or s ; in addition, non-parabolicity of the semiconductor conduction band should add additional curvature to the BEEM spectrum at higher voltages, which may appear as a change in the effective barrier parameters. These considerations, however, do not change the quality of the fit to the threshold shape or location. Only the on-axis X minimum is considered when calculating theoretical spectra; the angles of the critical cones for the off-axis minima are so large (about 43 degrees) that the tunneling formalism which is used does not provide appreciable current into these large angles.

It can be seen that the threshold shape is especially well fit by theory, and that the predicted quadratic behavior is present. A much more sensitive test of this agreement may be performed by a comparison of the derivatives, dI_c/dV , of the experimental and theoretical spectra. These are shown in Figure XX(2) for the spectra in Figure XX(1). This agreement provides a powerful test of the assumptions made in the BEEM theory. In particular, k_t conservation dictates a quadratic threshold. The removal of this

conservation law at the interface can be simulated theoretically by allowing all electrons of sufficient total energy to be collected. The shape of the spectrum generated by such an assumption is drastically different from that of the conventional theory. In particular, such a spectrum displays a *linear* threshold, in contradiction with experiment. For comparison, the best fit of such a spectrum to the data of Figure XX(1) is shown in Figure XX(3); the disagreement is pronounced.

Several observations may be made concerning the spatial variation of Au/n-Si(100) spectra. Many individual spectra were obtained for many samples, reflecting a small spread of Schottky barrier heights, from 0.75 eV to 0.82 eV. The variation in R values was also small, with differences between spectra of no more than a factor of three. Some level of variation in the magnitude of I_c (of which R is a measure) is expected from variations in base electrode thickness from point to point. This homogeneity has been probed directly by BEEM interface imaging, and will be discussed in the next section.

One capability which BEEM provides is the ability to determine attenuation lengths of hot carriers in metals and semiconductors. This method provides a straightforward way of determining attenuation lengths which are not weighted toward the thinnest base regions, as would be the case for conventional measurements on large area interfaces. The simplest experiment consists of measuring collector current as a function of base thickness. The effective attenuation length is then given by

$$I_c = I_0 e^{-t/\lambda} \tag{17}$$

where t is the base thickness and λ is the attenuation length. Complete I_c -V spectra of Au/n-Si(100) were obtained and fits performed to obtain R values, which provide a voltage-independent measure of the magnitude of I_c . A semilogarithmic plot of R

versus t is shown in Figure XX(4). The expected exponential relationship is apparent, and the derived attenuation length is 128 \AA . To obtain the data points which are shown, the R values of many spectra were averaged at each thickness and different samples of each thickness were fabricated, in order to account for spatial variations of base thickness about its average value. Note that this yields a true average which does not weight thin base regions more heavily than others.

While Au/Si provides an interface that is relatively well-characterized, the Au/n-GaAs(100) interface system is considerably more complex. In addition to the direct minimum at Γ , the conduction band has two satellite minima, at the L and X points of the zone. In addition to the more complicated conduction band structure, reproducibility of interface characteristics is known to be difficult. A representative BEEM spectrum and fit to theory are shown in Figure XX(5). In this case, the data is fit with a three-threshold model, in which three separate R values are also allowed to vary. Vacuum barrier parameters $\Phi = 3 \text{ eV}$ and $s = 15 \text{ \AA}$ are also used for this case.

The multiple-threshold nature of the Au/n-GaAs spectrum is clear; the derivative of data and theory, given in Figure XX(6), makes the three thresholds even more apparent. A free fit of the threshold locations yields $E_{\Gamma} - E_{\text{F}} = 0.89 \text{ eV}$, $E_{\text{L}} - E_{\text{F}} = 1.18 \text{ eV}$, and $E_{\text{X}} - E_{\text{F}} = 1.36 \text{ eV}$. These values are in agreement with the accepted relative locations $E_{\text{L}} - E_{\text{F}} = 0.29 \text{ eV}$ and $E_{\text{X}} - E_{\text{F}} = 0.48 \text{ eV}$. The relative R values for the three minima indicate a somewhat wider angular distribution than planar tunneling predicts, since the critical cones for the L minima are at about 36 degrees. This may be due to the tunneling process or to elastic scattering of the electrons in the base, although the expected R values are complicated to calculate without knowing details of the scattering. For this case, also, the off-axis X minima are neglected, due to the large angle for the critical cones of about 55 degrees.

Au/n-GaAs(100) interface, for which a typical image pair is shown in Figure XX(9). The variation from dark to light in the interface image represents about two orders of magnitude in collected current; the precise ratio is difficult to determine, since there is virtually no detectable current within the darkest areas. This large range of intensity values is typical of this interface system, and is too great to be explained by a simple thickness variation of the base electrode. Moreover, the variation in intensity is due primarily to a variation in R rather than to a change in threshold. Spectra taken within lower current areas where there is enough signal to determine thresholds do not indicate a systematic relationship to threshold position.

It has been demonstrated that interfaces formed both on melt-grown and MBE-grown GaAs substrates exhibit this heterogeneity, indicating that bulk defect density does not play a large part in the presence of this interface disorder. The heterogeneity also persists over a wide range of surface preparation conditions. Chemically cleaned GaAs substrates which were exposed to air prior to Au deposition exhibit this behavior; a careful chemical cleaning of the GaAs substrate in flowing nitrogen gas followed by direct transfer to the Au deposition chamber also produces such interfaces, even though XPS shows them to be oxide-free. This is an indication that the interface defect structure is not simply the result of surface contamination.

GaAs is known to dissociate at the interface of a Au/GaAs contact; while the Ga is soluble in Au and tends to migrate to the Au surface, As is insoluble and remains at the interface. These low-current areas actually dominate the Au/GaAs interface, and are interpreted in terms of interracial islands of As created by GaAs dissociation and Ga migration. The experimental results indicate that this diffusion process dominates the interface formation process in the Au/GaAs(100) system.

The spatial variation of spectra for the Au/n-GaAs(100) interfaces much greater than for Au/n-Si(100). Measured SB heights for Au/GaAs range from 0.8 eV to 1.0 eV. In addition, the range of R values is as much as two orders of magnitude, much greater than can be explained by a variation in Au thickness. This heterogeneity was also probed by interface imaging, and will be addressed in the following section.

7. IMAGING RESULTS

Interface imaging is made possible by the capability of the STM to scan a tip across the sample, and by the highly localized electron beam which is injected by the tip. The correspondingly high resolution at the interface has already been discussed theoretically. An interface image is acquired simultaneously with an STM topograph by measuring I_c at each point on the surface during the scan, while at a tip bias voltage in excess of threshold. Examples of the experimental results will be presented here.

It was mentioned in the last section that I_c -V spectra for Au/n-Si(100) show only a small variation from point to point. This variation was probed directly by BEEM imaging, and a representative surface topograph and interface image for this system are shown in Figure XX(7). The average value of I_c over the image is 18 pA, while the RMS variation is only 0.7 pA, which is on the order of the noise level in the acquisition apparatus. This image therefore represents an extremely uniform interface. Spectra were acquired at several locations across the image, and these spectra are plotted in Figure XX(8). The average value of I_c for these spectra at the imaging voltage of 1.5 V is 18.0 pA, in good agreement with the image average. It is notable that the dependence of the collected current on the surface Au topography is quite weak.

In marked contrast to this uniformity is the heterogeneity observed for the

8. HOLE SPECTROSCOPY RESULTS

Ballistic hole spectroscopy was first performed on the SB systems which were previously probed by BEEM, allowing a characterization of the interface valence band structure of these structures. As mentioned in the theoretical discussion, a p--type semiconductor collector is used for ballistic hole spectroscopy, and the typically low barrier heights for p--type semiconductors necessitate low--temperature measurements. A ballistic hole spectrum for Au/p--Si(100) obtained at 77K is shown in Figure XX(10). Also shown is a fit of the ballistic hole theory to the data,. The sign of the collected current is not arbitrary; a negative sign for the current indicates the collection of holes. The Schottky barrier height V_b for this system is measured to be 0,35 eV, with only a small spread in this value from point to point. It should be mentioned that the n and p barrier heights measured at 77K add to 1.17 eV, which agrees well with the Si 77K bandgap value of 1.16 eV.

Derivatives of both the electron and hole spectra, both obtained at 77K, are shown in Figure XX(11). The derivative of the ballistic hole spectrum maximizes and turns over more quickly than that of the electron spectrum. This can be interpreted in terms of the asymmetry between the collected distributions for electron and hole injection. For the hole case, the additional current per unit voltage is decreasing, causing the I_c --V spectrum to inflect more quickly. A second feature to notice is the extremely sharp thresholds in the derivatives, which is provided by data acquisition at low temperature.

For this and other ballistic hole spectra, R values are larger than for the corresponding electron spectra. In addition, the best fits to the data are obtained for the vacuum gap parameters $\Phi = 3$ eV and $s = 8$ Å, whereas the values $\Phi = 3$ eV, $s = 15$ Å were used for electron spectra. This may be an indication that the tunneling formalism being used does

not describe the energy distribution of tunneling electrons accurately, at least for tunneling from sample to tip. Ballistic hole spectroscopy is more sensitive to the details of the tunneling distribution than is ballistic electron spectroscopy, since the collected carriers come from the tail of the tunneling distribution. However, as with BEEM spectroscopy, these considerations do not affect the quality of the fit near threshold or the determination of the interface barrier height.

Although the conduction bands of Si and GaAs are quite different, the valence band structures are similar. For both semiconductors, the valence band system is composed of three separate bands, the light-hole, heavy-hole, and split-off bands. The light- and heavy-hole bands are degenerate at the center of the Brillouin zone and define the p-type Schottky barrier; away from the zone center, the mass of the light hole band increases until the two bands are of essentially equal mass, but split by a small energy difference. The third band is non-degenerate at the zone center due to spin-orbit splitting,

In the case of Au/p-Si(100), this light-hole/heavy-hole splitting is only about 30 meV, and is not resolved with the present apparatus; however, this is not the case for Au/p-GaAs(100). A ballistic hole spectrum of Au/p-GaAs(100) is shown in Figure XX(1 2). Also plotted are two theoretical curves. The first considers only a single threshold at the valence band edge; the second includes the light-hole band, with the approximation that this band changes abruptly from its light-hole mass to the heavy-hole mass away from the zone center. [Ref: the point of transition is obtained from Figure 47 of reference ZZ] It is apparent that this second fit agrees well with the threshold shape of the experimental spectrum, while the first fit is poor at threshold. The measured barrier height is 0.70 eV, while the effective splitting of the light- and heavy-hole band away from the zone center is about 100 meV, in good agreement with current values of this splitting obtained by other methods.

It should be noted that the simple phase space model which has been used to analyze electron and hole spectra thus far would not predict the observation of the light hole band in the Au/p-GaAs data. The phase space for collection by the light-hole band is completely within that for the heavy-hole band; therefore, there is no additional phase space for collection when the onset of the light-hole band is reached. The assumption of the phase-space model, that all carriers within the critical cone are collected, is therefore inappropriate here; this would not allow additional current due to the light-hole band. The additional current is expected, however, if there is quantum-mechanical reflection at the interface which allows only a portion of the carriers within the critical cone to be collected. A second channel for collection would then produce an increase in current. The particular form of the QMR depends on the potential profile and mass change across the interface. In fact, a mass change alone will produce a constant QMR term, even in the absence of a change in potential. The observation of both bands in the ballistic hole spectrum, then, is a direct indication of QMR for this interface system.

A footnote to this discussion is that the split-off bands for both Si and GaAs should in principle be observable. However, the masses of these bands are smaller than those of the heavy-hole bands, and the increase in current due to them is difficult to detect. Their contribution to the I_c - V spectrum is not observed, but AC detection methods should resolve these bands.

9. SCATTERING SPECTROSCOPY RESULTS

The first application of the carrier scattering spectroscopy discussed previously was to the interface systems which have been investigated by BEEM: Au/Si(100) and Au/GaAs(100). The importance of these interfaces has already been emphasized; a characterization of transport within the electrodes themselves is also of great importance

to a complete understanding of the entire transport process. In addition, analysis of the results of this scattering spectroscopy is aided by the previous characterization of interface transport and the collection process, which is provided by the ballistic spectroscopes which have already been discussed.

Figure XX(13) displays two spectra obtained for Au/p-Si(100). The spectrum at positive tip voltage is a ballistic hole spectrum similar to that in Figure XX(10), with a threshold which yields a Schottky barrier height of 0.35 eV. Shown at negative tip bias is a spectrum of holes created by carrier scattering. In this case, the negative tip voltage injects ballistic electrons into the sample, some of which scatter with equilibrium electrons in the base and result in the creation of secondary electron-hole pairs. The secondary electrons eventually decay to the Fermi level, but some of the secondary holes may be collected by the Si valence band before they thermalize. The plotted spectrum is due to these holes. Also shown is an expanded version of this scattering spectrum. It is clear that the spectral shapes and the magnitudes of the currents are quite different for the ballistic and scattering spectra. A theoretical curve is also shown, which was fit to the data by adjustment of only an overall scaling factor reflecting the magnitude of the current. Agreement with experiment is excellent. The scattering spectrum also exhibits a threshold at 0.35 eV, the value of the Schottky barrier height for this system. This observation of collected current well below the Si conduction band edge ($eV_b = 0.82$ eV) rules out any processes involving transport in the Si conduction band.

A similar experiment may also be performed for Au on p-GaAs(100). Since the barrier height for this interface is roughly twice that of Au/p-Si, it provides a good test of the theoretical description developed for the process. As shown in Figure XX(1 4), the spectra are qualitatively similar to those for Si. This is to be expected, since this spectroscopy is primarily a probe of processes with in base layer, independent of the collector. However,

the measured spectra do reflect aspects of the particular collector electrode used. Most noticeably, the threshold is determined by the Au/p-GaAs Schottky barrier height, 0.70 eV. In addition, the current of scattered carriers for this system is smaller than that for Au/p-Si, for equivalent voltages in excess of threshold. This is due to the smaller fraction of phase space available for scattering and collection, and the ratios of the currents for the two systems agrees well with that predicted by theory. This agreement indicates that there is no large interface-specific contribution to the scattering process itself.

This scattering spectroscopy has also been performed for n-type collectors. Here, injected ballistic holes may scatter with equilibrium electrons in the base and create electron-hole pairs, and the secondary electrons are collected in the conduction band of the n-type semiconductor. Figure XX(15) shows ballistic and scattering spectra for Au/n-Si(100). The threshold reflects the n-type Schottky barrier height of 0.82 eV. In this case, there is good agreement of the theory with the data near threshold; however, the measured collector current increases more rapidly at higher voltages than the theory predicts. The overall magnitude of the current is also surprisingly high, almost two orders of magnitude higher than expected from the theory. This may indicate that the initial electron distribution is not correctly described by planar tunneling, a possibility which was also raised earlier in connection with ballistic hole spectroscopy.

10. CONCLUSIONS

This chapter has covered the basic concepts of ballistic carrier spectroscopies using the STM, as well as an extension to the study of non-ballistic processes. BEEM and its related techniques are extremely powerful probes of subsurface interfaces and of carrier transport through materials and across these interfaces. BEEM provides the most precise method available for the determination of Schottky barrier heights, and in addition is sensitive to other characteristics of the interface band structure, such as effective mass and satellite conduction minima. The implementation of BEEM using STM is a vital aspect of the method, since the highly localized electron injection enables a corresponding spatial resolution of interface properties. This implementation therefore provides an interface imaging capability, which has been used to reveal hitherto unknown heterogeneity at semiconductor interfaces. The theoretical description of BEEM spectroscopy has been discussed, as well as the implications of this theory for interface imaging resolution.

The precision of barrier height measurements allows the determination of small changes in barrier height due to such factors as strain or temperature change. Such measurements are one important means for evaluating theories of interface formation.

BEEM also provides information on fundamental questions regarding carrier transport. For instance, spectroscopy of interfaces formed on semiconductors with off-axis minima should yield insight concerning the tunneling distribution, in E and k , of electrons in a tip-plane geometry, as well as the much-argued notion of conservation of k_t across a real interface. Two of the methods for probing carrier transport through materials have been presented in this chapter. The first, using conventional BEEM, involves the measurement of collector current as a function of base thickness and a determination of a carrier

attenuation length. This measurement may also be performed for the case of off-axis collector band minima, which should elucidate the contributions of elastic and inelastic scattering to the measured attenuation length.

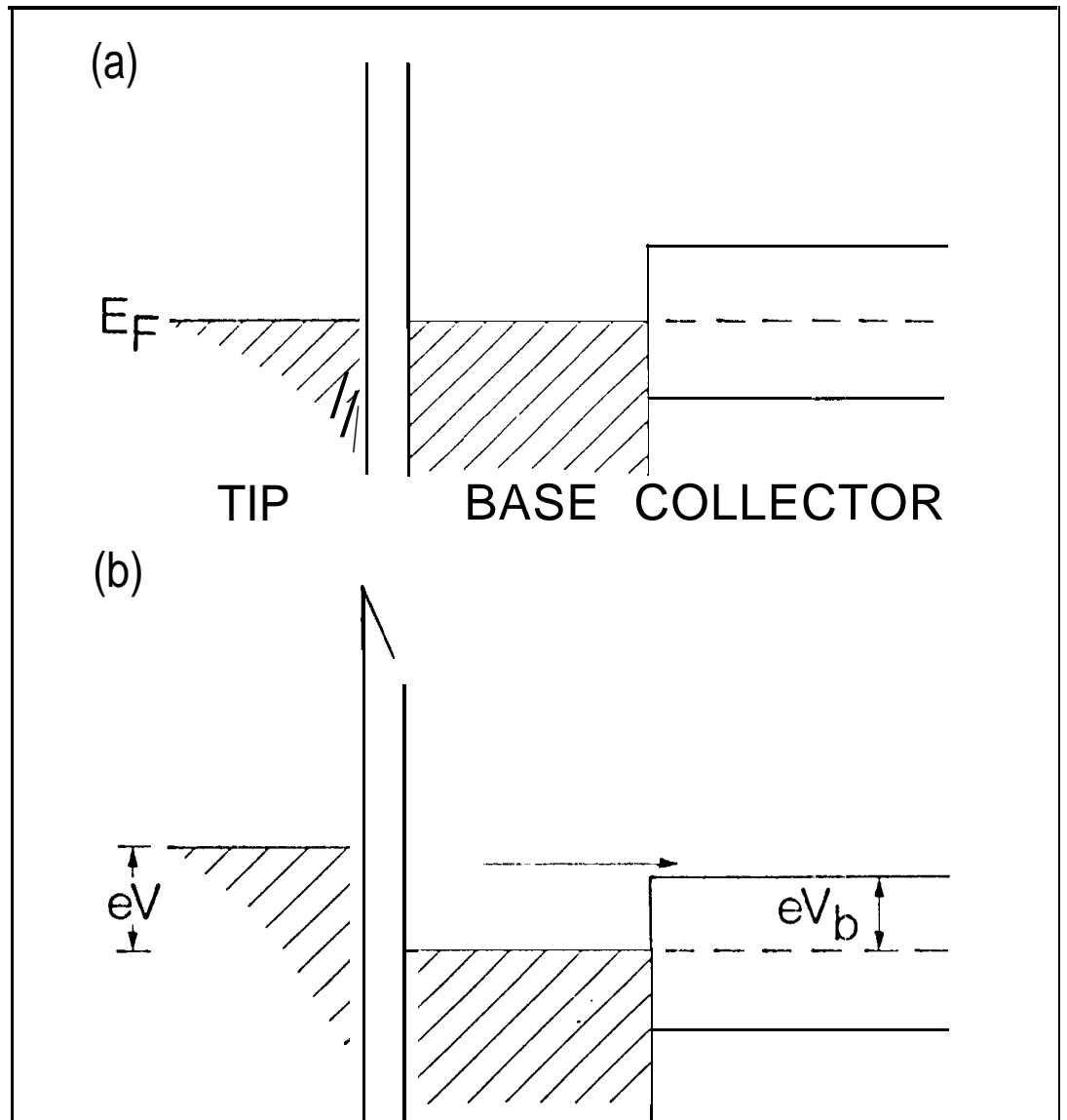
The second method for the investigation carrier transport involves the use of the spectroscopy discussed in this chapter. This spectroscopy allows the first direct probe of carrier-carrier scattering in materials, and can also be performed as a function of base thickness, temperature and with off-axis collectors to provide a wealth of data on carrier scattering mechanisms. The theoretical treatment for this process yields good agreement with experiment and, as in the case of BEM theory, may be built upon to incorporate more complicated processes.

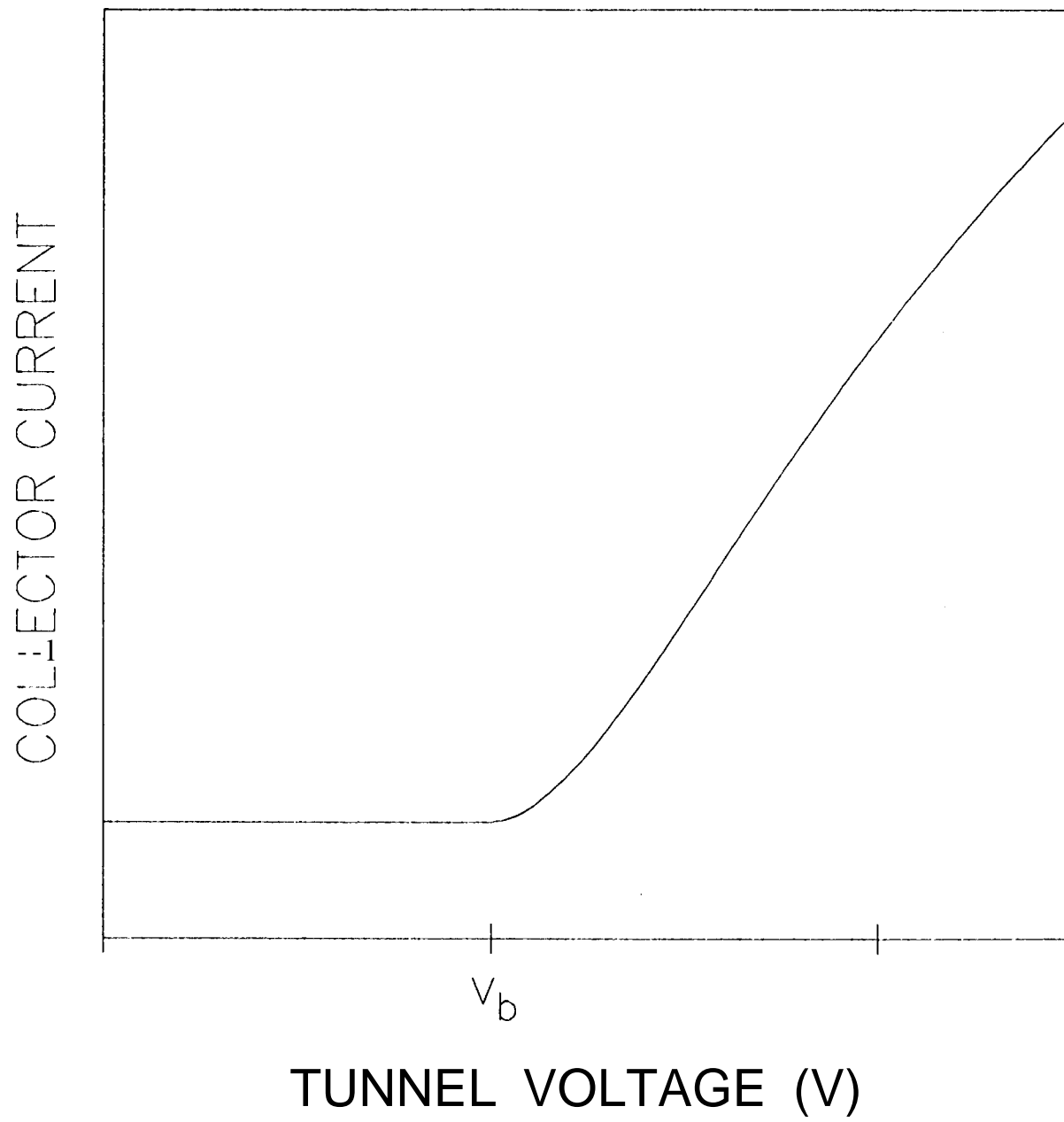
ACKNOWLEDGMENT

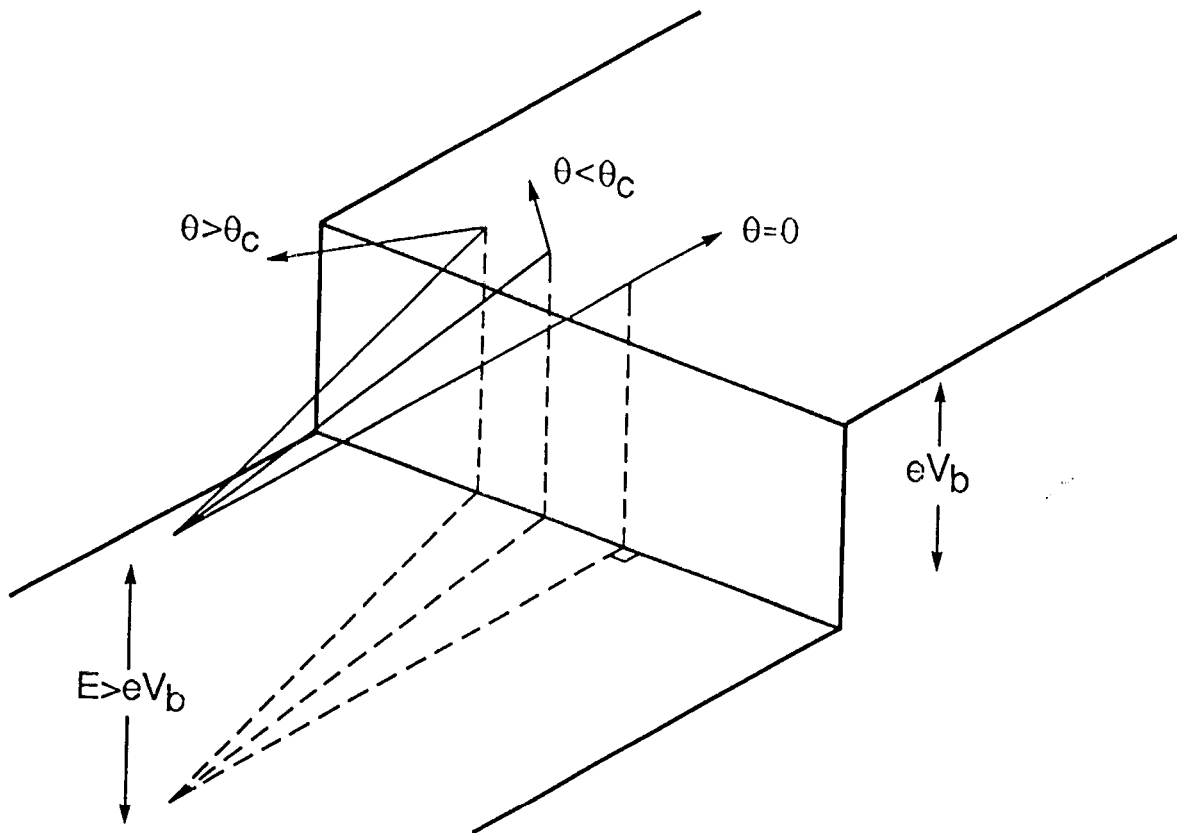
The work described in this paper was performed by the Center for Space Microelectronics Technology, Jet Propulsion Laboratory, California, Institute of Technology, and was sponsored by the Office of Naval Research and the Strategic Defense Initiative Organization / Innovative Science and Technology Office through an agreement with the National Aeronautics and Space Administration (NASA).

RESULTS FIGURES

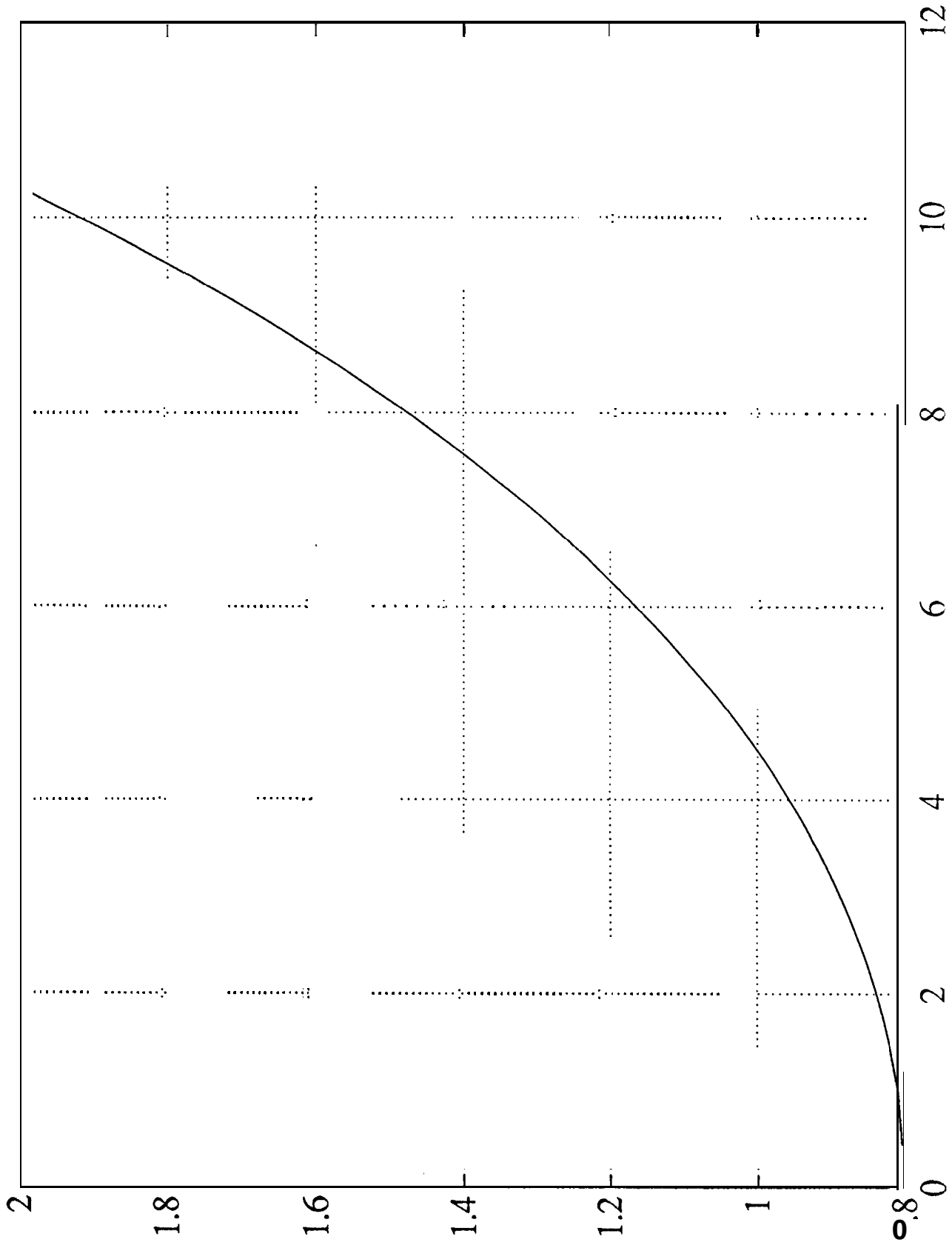
- Figure 1 Au/Si spectrum / fit
- Figure 2 derivative spectrum and fit for Au/Si
- Figure 3 nok,conservation fit
- Figure 4 attenuation length plot
- Figure 5 Au/GaAs spectrum and fit
- Figure 6 derivative spectrum and fit for Au/GaAs
- Figure 7 Images of Au/Si
- Figure 8 Spectra corresponding to Fig 7 image
- Figure 9 Images of Au/GaAs
- Figure 10 Hole spectrum of Au/Si with fit
- Figure 11 Derivatives of electron and hole spectra for Au/Si
- Figure 12 Hole spectrum of Au/GaAs with fits
- Figure 13 Ballistic and scattering spectra, Au/p-Si(100), with fit
- Figure 14 Ballistic and scattering spectra, Au/p-GaAs(100), with fit
- Figure 15 Ballistic and scattering spectra, Au/n-Si(100), with fit





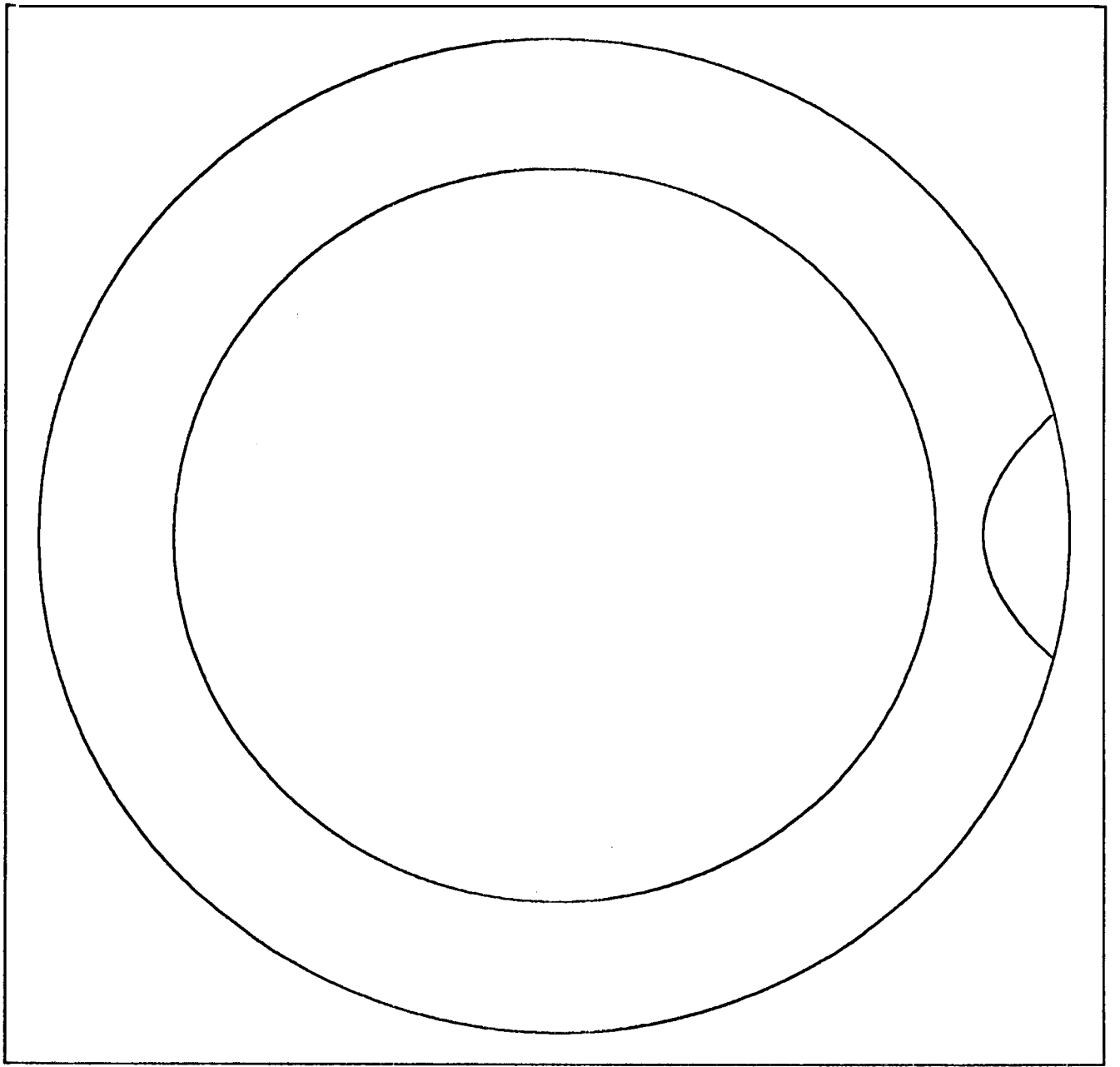


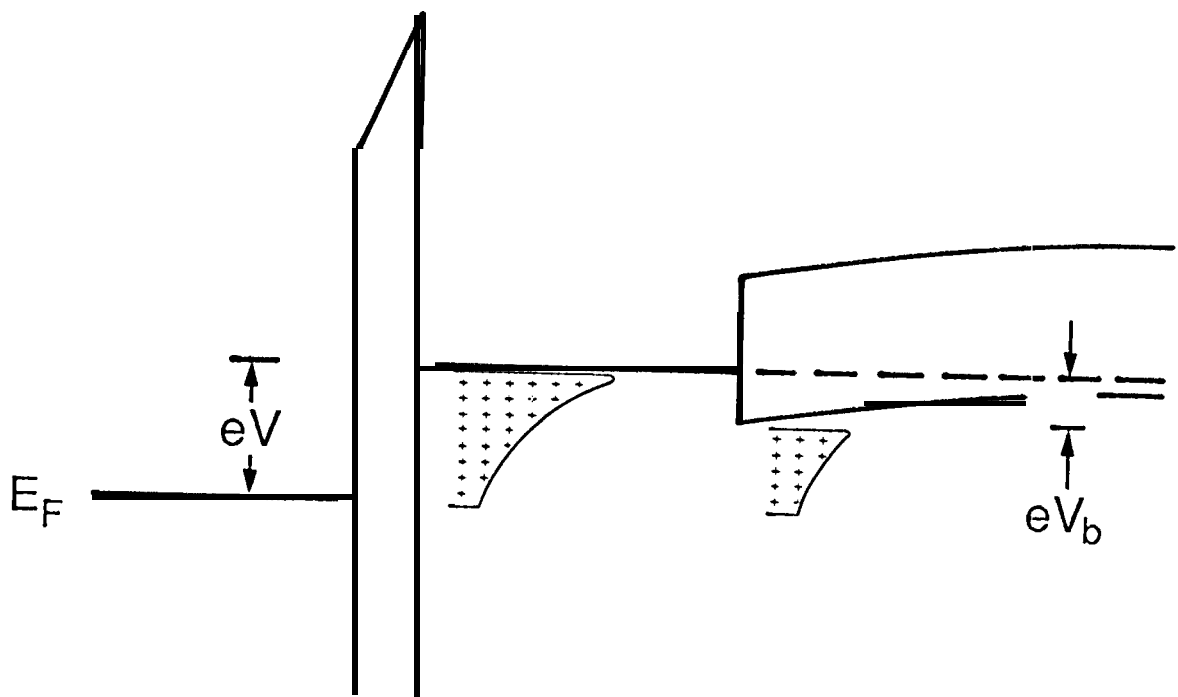
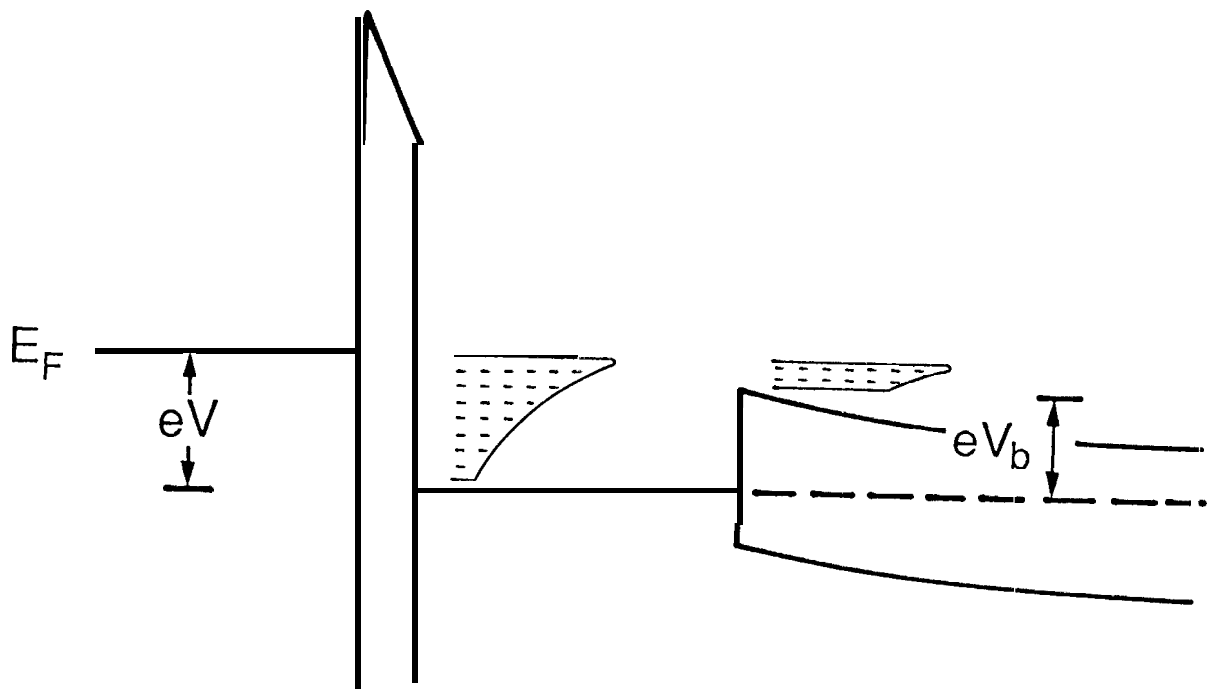
$mt/m=.2, Vb=.8, Ef=5.5$

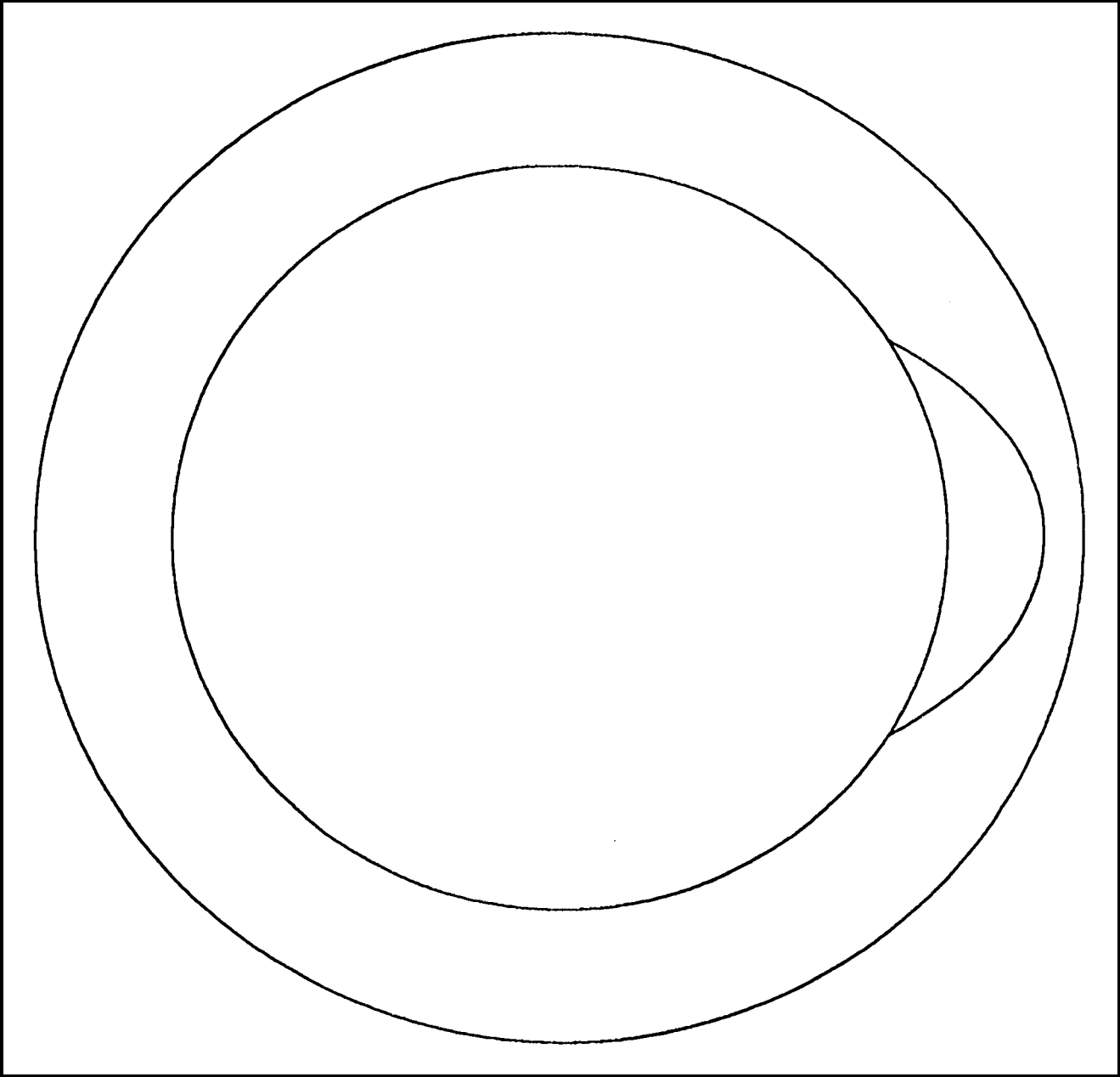


Critical angle (degrees)

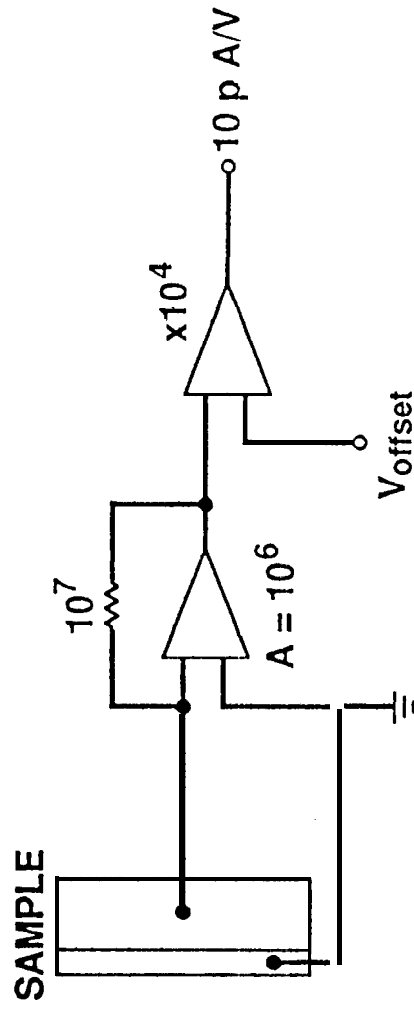
(A) A



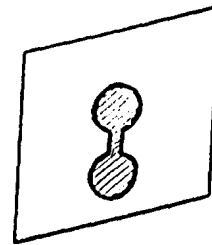
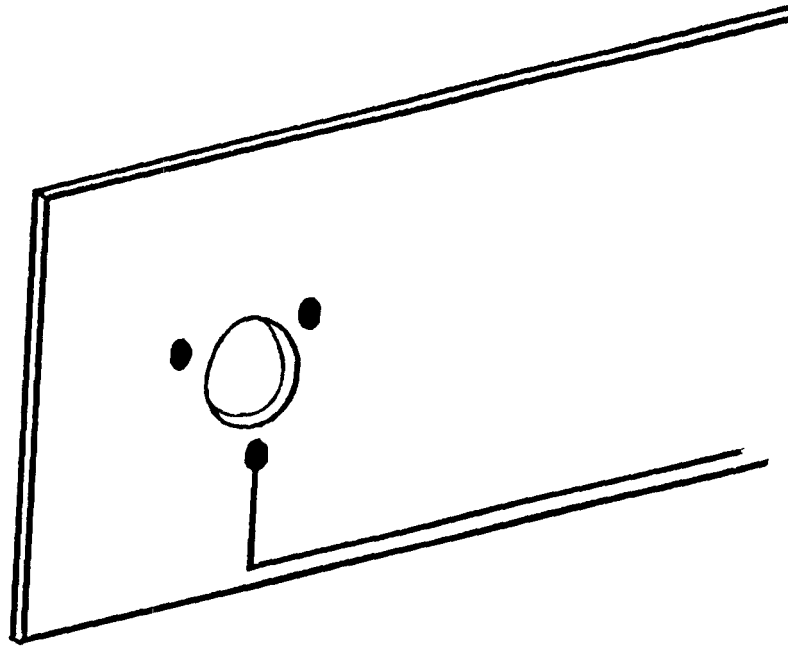


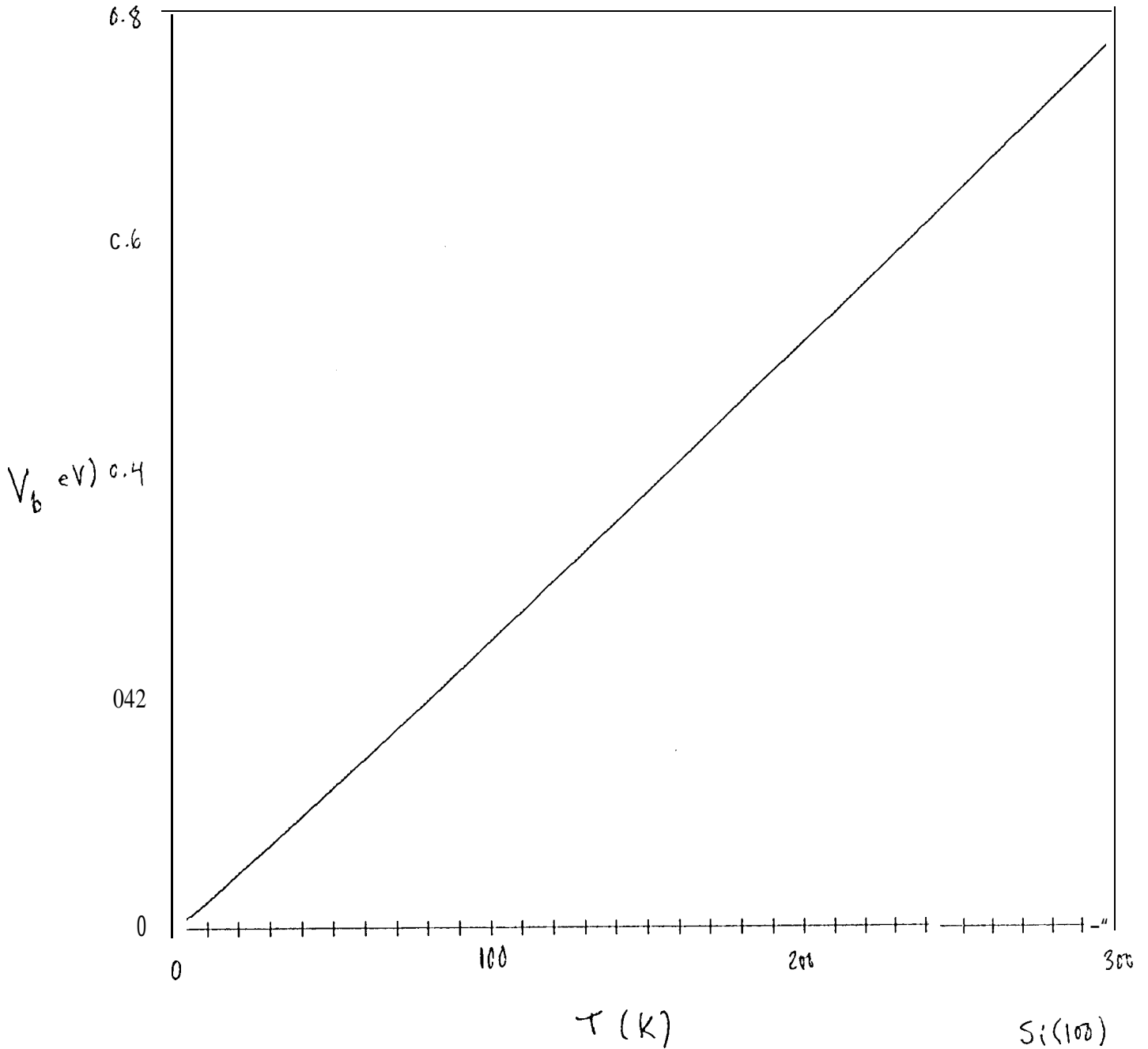


JPL COLLECTOR CURRENT \approx NT AMPLIFIER



BEEP SAMPLE MOUNTING





V_b (eV) 0.4

T (K)

Si(100)
 $A^* = 252$
 $a = 0.1 \text{ cm}^2$

Au-Si(100)

